

Modeling the Unseen: Inference and Reconstruction in Accretion Disk Physics

Makoto Uemura^{a,*}

^a*Hiroshima Astrophysical Science Center, Hiroshima University,
Kagamiyama 1-3-1, Higashi-Hiroshima, Japan*

E-mail: uemuram@hiroshima-u.ac.jp

Recent advances in inference techniques have opened new pathways for unveiling the hidden structures and dynamics of accretion disks. By integrating physical insight with modern statistical and machine learning tools, it is now possible to infer key properties of systems where direct observation is limited or impossible. This article surveys a series of studies illustrating this trend. First, we address ill-posed inverse problems, where sparse regularization enables the reconstruction of disk structures from indirect observables, ranging from power-spectrum estimations and Doppler tomograms to black hole shadow imaging. Second, we explore time-series analysis techniques based on state-space modeling, which separate spectral components in X-ray binaries. Third, we present dynamic mode decomposition applied to hydrodynamical simulations of accretion disks, revealing eccentric and $m = 3$ modes associated with the disk reaching the 3:1 resonance. Fourth, we demonstrate an information-theoretic framework for autonomous observational decision-making, as implemented in real-time follow-up observations of cataclysmic variables with the Kanata telescope. These examples highlight how data-driven modeling can reveal unseen aspects of accretion phenomena across diverse astrophysical contexts and timescales.

*87th Fujihara Seminar: The 50th Anniversary Workshop of the Disk Instability Model in Compact Binary Stars (DIM50TH2025)
22-26 September 2025
Tomakomai, Japan*

*Speaker

1. Introduction

Understanding the physics of accretion disks often requires inferring what cannot be directly observed. Their complex structures and temporal behaviors must be reconstructed from limited data. In recent years, advances in statistical inference and machine learning have provided new tools for this purpose. In this article, we present a series of studies — mainly from our recent work — that explore how such modern methodologies can be applied to uncover the hidden aspects of accretion disk systems.

The following sections are organized as follows. Section 2 introduces applications of tomography and inverse-problem approaches. Section 3 focuses on time-series analysis. In Section 4, methods of unsupervised feature extraction are presented. Section 5 describes our recent work on an autonomous observation system including machine classification. Finally, Section 6 provides a summary of this article.

2. Tomography and inverse problems

Tomographic techniques such as Doppler tomography and eclipse mapping have played a central role in understanding accretion disks in close binary systems [1, 2]. In these methods, the observed data vector \mathbf{y} is modeled as a linear transformation of the unknown disk structure \mathbf{x} through a known matrix \mathbf{A} , namely $\mathbf{y} = \mathbf{A}\mathbf{x}$. Estimating \mathbf{x} from \mathbf{y} constitutes an inverse problem. Because the dimension of \mathbf{y} is often smaller than that of \mathbf{x} , a unique solution cannot be obtained by a simple least-squares approach. Instead, a regularized least-squares (RLS) method is adopted,

$$\hat{\mathbf{x}} = \arg \min_{\mathbf{x}} \|\mathbf{y} - \mathbf{A}\mathbf{x}\|_2^2 + \lambda\Phi(\mathbf{x}), \quad (1)$$

where $\Phi(\mathbf{x})$ is a regularization term and λ is its weighting coefficient. A well-known example is the maximum entropy method (MEM), in which $\Phi(\mathbf{x}) = -\sum x_i \ln(x_i/m_i)$, with m_i representing a default map.

In recent years, a variety of alternative regularization functions $\Phi(\mathbf{x})$ have been developed. One of the most widely used modern approaches is the sparse regularization, where sparsity is imposed through the ℓ_1 norm. LASSO (Least Absolute Shrinkage and Selection Operator; [3]) uses $\Phi(\mathbf{x}) = \|\mathbf{x}\|_1 = \sum |x_i|$, leading to sparse solutions in which only a small number of elements of \mathbf{x} remain non-zero.

Figure 1 illustrates a LASSO application to power spectrum estimation [4]. Here, \mathbf{y} , \mathbf{A} , and \mathbf{x} represent the observed light curve, the inverse Fourier transform matrix, and the Fourier coefficients, respectively. The true spectrum (left) is sparse, with only six non-zero components. The complete light curve generated from this spectrum is shown in gray (middle), while the actual observed data are limited to the black points. This incomplete sampling produces a "dirty" spectrum (gray, right) containing many alias components. LASSO effectively removes the aliases and recovers the correct components (black curve), closely reproducing the true spectrum.

While the ℓ_1 regularization enforces sparsity in \mathbf{x} , another useful form is the total variation (TV) regularization, defined as $\Phi(\mathbf{x}) = \sum |x_{i+1} - x_i|$, which promotes sparsity in the gradient of \mathbf{x} . This approach, known as total variation minimization (TVM), favors piecewise-smooth reconstructions while preserving sharp edges. Figure 2 shows TVM-based Doppler maps of the dwarf nova WZ Sge

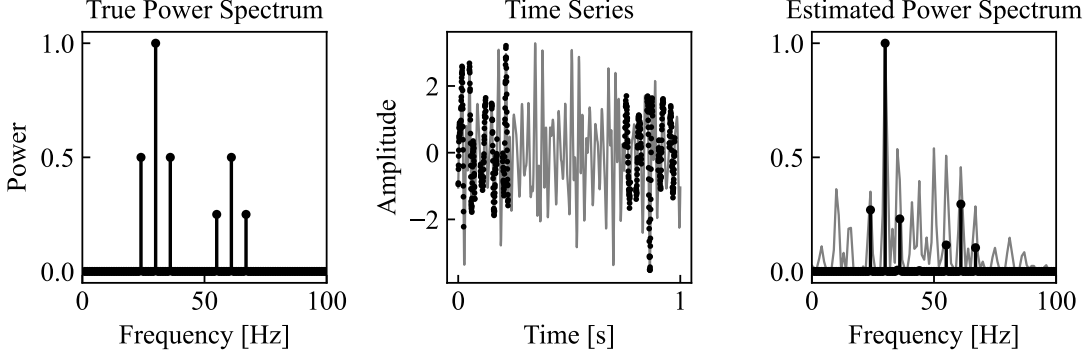


Figure 1: LASSO-based estimation of a power spectrum. Left: true spectrum. Middle: complete light curve (gray) and observed data (black dots). Right: dirty spectrum from incomplete data (gray) and LASSO reconstruction (black).

during outburst [5]. From left to right, the regularization coefficient λ decreases. Large λ values yield overly smoothed maps, whereas small λ produces overfitting to the data. Nevertheless, key structural features are consistently recovered: a bright spot near the secondary star and an asymmetric, elliptical ring characteristic of an accretion disk. MEM inherently favors smooth brightness distributions without explicitly modeling spatial relationships between pixels, whereas TVM directly compares neighboring pixels, providing greater flexibility in capturing local features.

Another recent and prominent success in astronomical imaging is the reconstruction of black hole shadows by the Event Horizon Telescope (EHT). Honma et al. (2014) proposed the use of LASSO for very long baseline interferometry (VLBI) imaging and demonstrated its ability to achieve super-resolution [6]. The imaging technique was later extended in the EHT analysis of M87*, which employed a combination of three regularization terms: $\lambda_1 |\mathbf{x}|_1 + \lambda_2 \text{TV}(\mathbf{x}) + \lambda_3 \text{TSV}(\mathbf{x})$, where the third term, total squared variation (TSV), promotes local smoothness [7]. For a 2D image $\mathbf{x} = \{x_{i,j}\}$, TSV is defined as $\text{TSV}(\mathbf{x}) = \sum_{i,j} (|x_{i+1,j} - x_{i,j}|^2 + |x_{i,j+1} - x_{i,j}|^2)$. The combination of these three types of regularization allows for highly flexible reconstructions, though balancing the

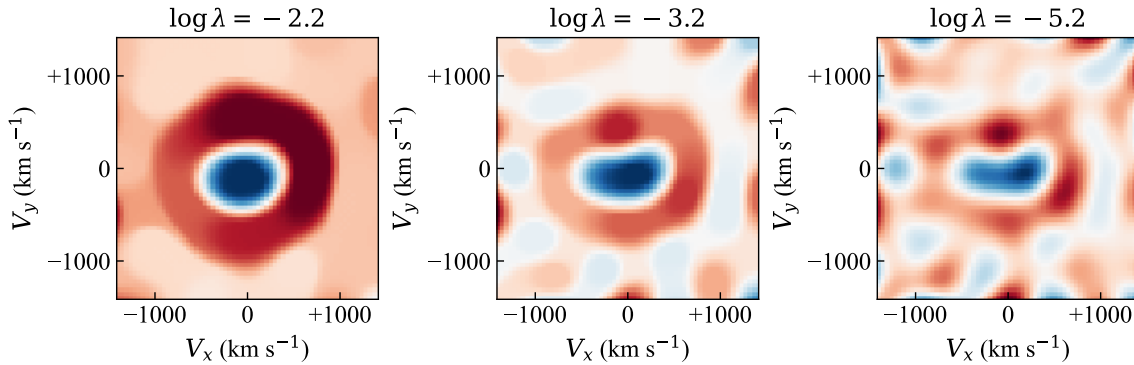


Figure 2: Doppler maps of the dwarf nova WZ Sge in outburst reconstructed by total variation minimization (TVM). Left, middle, and right panels correspond to large, optimal, and small λ values, respectively.

three coefficients λ_1 , λ_2 , and λ_3 poses a practical challenge.

3. Time-series analysis

In this section, we focus on black hole X-ray binaries (BHXBs) and discuss how their rapid variability provides insights into accretion physics. A traditional approach to studying variability is to compute power spectra and cross spectra between different energy bands. However, X-ray light curves often consist of emissions originating from multiple regions - such as the accretion disk, the corona, and reflected components. Analyzing the light curves without separating these components can lead to misleading interpretations [8].

To address this issue, a state-space modeling approach has been applied to the X-ray data of MAXI J1820 + 070 [9]. In the low/hard state, its X-ray spectrum can be decomposed into three major components: a power-law, a disk blackbody, and a soft excess. The observed light curves arise as a mixture of these components. The model aims to decompose their contributions and directly characterize their temporal behavior and causal relationships.

The model assumes three latent variables, $\mathbf{x}_t = (x_t^{(1)}, x_t^{(2)}, x_t^{(3)})$, representing the temporal intensities of the power-law, disk blackbody, and soft excess components, respectively. Their evolution is described by a second-order vector autoregressive (VAR) process:

$$\mathbf{x}_t = \mathbf{A}_1 \mathbf{x}_{t-1} + \mathbf{A}_2 \mathbf{x}_{t-2} + \mathbf{v}_t, \quad (2)$$

where \mathbf{v}_t denotes Gaussian noise, $\mathbf{v}_t \sim \mathcal{N}(0, \mathbf{I})$. The matrices \mathbf{A}_1 and \mathbf{A}_2 are 3×3 coefficient matrices describing the dynamical relationships between components. The previous study evaluated AIC for the VAR models with orders $p = 1-50$, and found that $p = 2$, that is, the second-order VAR model is the best for the data [9].

The observed light curves in five energy bands, $\mathbf{y}_t = (y_t^{(1)}, \dots, y_t^{(5)})$, are modeled as linear combinations of these latent variables:

$$\mathbf{y}_t = \mathbf{H} \mathbf{x}_t + \mathbf{w}_t, \quad (3)$$

where \mathbf{w}_t represents measurement noise, $\mathbf{w}_t \sim \mathcal{N}(0, \mathbf{L})$. The observation matrix $\mathbf{H} \in \mathbb{R}^{5 \times 3}$ encodes how each spectral component contributes to each energy band. The model assumes that only the power-law component, $x^{(1)}$, contributes to the hardest band ($y^{(1)}$), and that only the power-law and disk blackbody components contribute to the second-hardest band ($y^{(2)}$). Accordingly, \mathbf{H} is defined as:

$$\mathbf{H} = \begin{pmatrix} h_{11} & 0 & 0 \\ h_{21} & h_{22} & 0 \\ h_{31} & h_{32} & h_{33} \\ h_{41} & h_{42} & h_{43} \\ h_{51} & h_{52} & h_{53} \end{pmatrix} \quad (4)$$

In total, the model contains 45 free parameters: 18 VAR coefficients in \mathbf{A}_1 and \mathbf{A}_2 , 12 elements in \mathbf{H} , and 15 independent elements in the covariance matrix \mathbf{L} . Posterior distributions of all parameters are inferred using Markov chain Monte Carlo (MCMC) sampling. The latent states are inferred using a forward-backward Kalman smoothing algorithm.

A major advantage of the state-space modeling approach is that the VAR coefficients in \mathbf{A}_1 and \mathbf{A}_2 directly provide not only the temporal evolution of each component, but also their power spectra, individual power contributions, and cross-correlation functions. Using a 50-s dataset of MAXI J1820+070, the VAR-based approach revealed that the variability originates in the accretion disk, then propagates to the power-law component, presumably from a corona, with a time lag of about 0.1 s, and finally reaches the soft-excess component, likely associated with reflection from the outer disk regions, with no detectable lag (< 0.1 s) [9]. This propagation sequence is consistent with the prevailing picture of BHXBs, but importantly, our analysis provides the first direct confirmation of this scenario through explicit component separation. Further details of the results are presented in [9] and in the article by Noda et al. in this proceedings.

4. Unsupervised feature extraction

With the increasing dimensionality of modern datasets, visually identifying meaningful structures in the data has become challenging. As a result, data-driven methods for feature extraction and dimensionality reduction have become essential. Classical approaches such as Principal Component Analysis (PCA) extract orthogonal directions that maximize variance, while more recent nonlinear methods like Variational Autoencoders (VAEs) and Uniform Manifold Approximation and Projection (UMAP) provide flexible tools for learning latent representations and visualization.

In this section, we focus on the Dynamic Mode Decomposition (DMD) [10], a linear, data-driven technique that extracts coherent spatiotemporal structures from sequential data. DMD is particularly useful for analyzing fluid or hydrodynamic simulations, where the outputs are typically large and high-dimensional.

DMD assumes that the temporal evolution of the system from time step k to $k + 1$ follows linear dynamics, $\mathbf{x}_{k+1} = \mathbf{A}\mathbf{x}_k$, where $\mathbf{x}_k \in \mathbb{R}^N$ denotes the system state at time k . The dynamics over multiple steps can then be expressed as $\mathbf{x}_k = \mathbf{A}^k \mathbf{x}_0$, where \mathbf{x}_0 is the initial state. Let $\lambda_j \in \mathbb{C}$ and $\boldsymbol{\phi}_j \in \mathbb{R}^N$ ($j = 1, \dots, r$) be the eigenvalues and eigenvectors of \mathbf{A} , satisfying $\mathbf{A}\boldsymbol{\phi}_j = \lambda_j \boldsymbol{\phi}_j$. Defining the matrices, $\boldsymbol{\Phi} = (\boldsymbol{\phi}_1, \boldsymbol{\phi}_2, \dots, \boldsymbol{\phi}_r) \in \mathbb{R}^{N \times r}$ and $\boldsymbol{\Lambda} = \text{diag}(\lambda_1, \lambda_2, \dots, \lambda_r) \in \mathbb{C}^{r \times r}$, the eigenvalue equations for the leading r modes can be written as $\mathbf{A}\boldsymbol{\Phi} = \boldsymbol{\Phi}\boldsymbol{\Lambda}$. Using the pseudoinverse $\boldsymbol{\Phi}^\dagger$ of $\boldsymbol{\Phi}$, the system matrix can then be approximated as $\mathbf{A} \sim \boldsymbol{\Phi}\boldsymbol{\Lambda}\boldsymbol{\Phi}^\dagger$. The time evolution is then reconstructed as $\mathbf{x}_k \sim \boldsymbol{\Phi}\boldsymbol{\Lambda}^k \mathbf{b}$, where $\mathbf{b} = \boldsymbol{\Phi}^\dagger \mathbf{x}_0$. This yields the modal expansion

$$\mathbf{x}_k \sim \sum_{j=1}^r b_j \lambda_j^k \boldsymbol{\phi}_j. \quad (5)$$

Expressing $\lambda_j = |\lambda_j| e^{i\theta_j}$ and $b_j = |b_j| e^{i\psi_j}$, the evolution can be written as

$$\mathbf{x}_k \sim \sum_{j=1}^r |b_j| |\lambda_j|^k e^{i(\theta_j k + \psi_j)} \boldsymbol{\phi}_j. \quad (6)$$

The system matrix \mathbf{A} is estimated directly from data using a least-squares approach. Let $\mathbf{X}_0 = (\mathbf{x}_0, \mathbf{x}_1, \dots, \mathbf{x}_{T-1})$ and $\mathbf{X}_1 = (\mathbf{x}_1, \mathbf{x}_2, \dots, \mathbf{x}_T)$, so that $\mathbf{X}_1 = \mathbf{A}\mathbf{X}_0$. After estimating $\hat{\mathbf{A}} = \arg \min \|\mathbf{X}_1 - \mathbf{A}\mathbf{X}_0\|_2^2$, we typically obtain $\hat{\mathbf{A}} = \mathbf{X}_1 \mathbf{X}_0^\dagger$. However, the dimension of $\hat{\mathbf{A}}$ is often too large to compute its eigenvalues and eigenvectors directly. To reduce the dimensionality, we apply

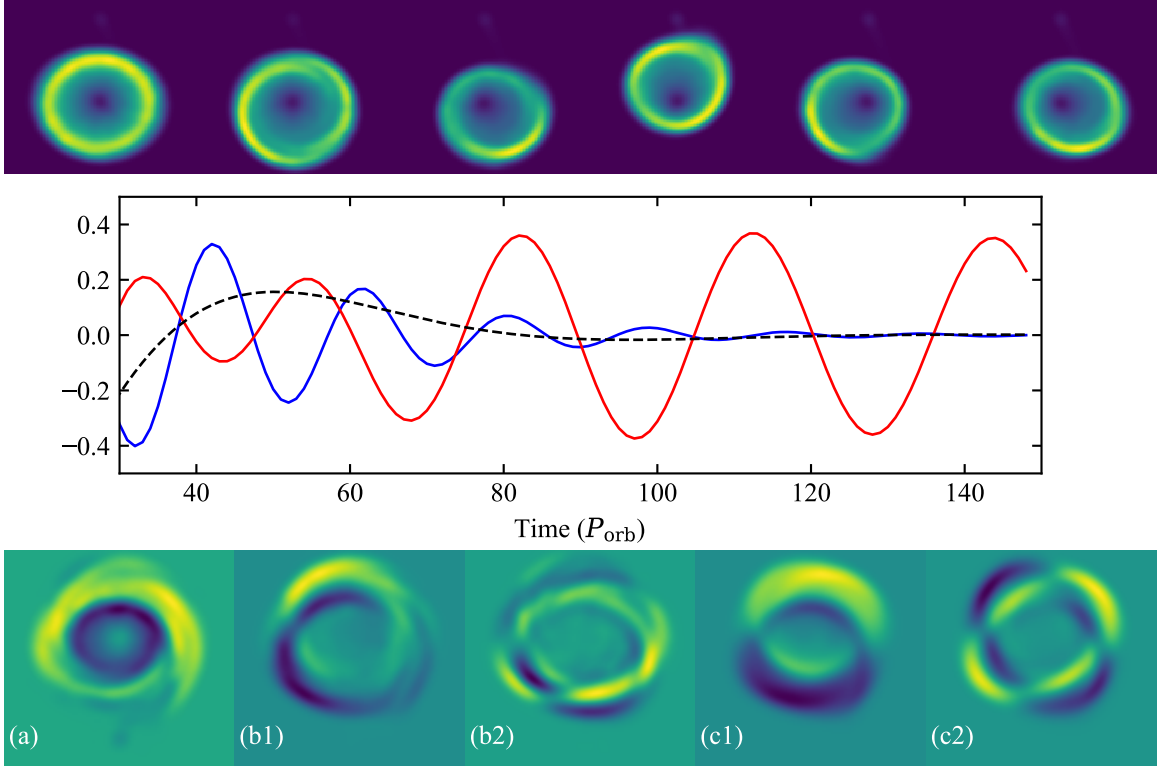


Figure 3: DMD for SPH simulation data of the 3:1 resonance in the accretion disk of cataclysmic variables. Top panels: SPH simulations of the disk at time 40, 60, 80, 100, 120, and 140 from left to right. Middle and bottom panels: Dynamics and DMD modes. The dashed curve shows the dynamics of mode (a). The blue curve shows the combined dynamics including modes (b1) and (b2). The red curve shows that including modes (c1) and (c2).

a truncated singular value decomposition (SVD) to X_0 as $X_0 = U_r \Sigma_r V_r^T$, where $U_r \in \mathbb{R}^{N \times r}$, $\Sigma_r = \text{diag}(\sigma_1, \dots, \sigma_r)$, and $V_r \in \mathbb{R}^{T \times r}$. We then project \hat{A} onto the subspace spanned by U_r . Let $F \in \mathbb{R}^{r \times r}$ denote this low-dimensional representation of \hat{A} : $F = U_r^T \hat{A} U_r$. Substituting $\hat{A} = X_1 X_0^\dagger$ and $X_0^\dagger = V_r \Sigma_r^{-1} U_r^T$, we obtain $F = U_r^T X_1 V_r \Sigma_r^{-1}$. This F is a small matrix whose eigenvalues $\lambda_{F,j}$ and eigenvectors $\phi_{F,j}$ can be readily computed. The eigenvalues and eigenvectors of the original system matrix \hat{A} are then given by $\lambda_j = \lambda_{F,j}$ and $\phi_j = U_r \phi_{F,j}$. This formulation allows the dominant spatial and temporal modes to be extracted efficiently, even from extremely large datasets.

Here, we apply DMD to smoothed particle hydrodynamics (SPH) simulation data of the 3:1 resonance in the accretion disk of cataclysmic variables (CVs) [11, 12]. In CVs with a low mass ratio ($q \lesssim 0.25$), the accretion disk can reach the 3:1 resonance radius. At this radius, tidal forces induce a resonance mode that interacts with the eccentric mode, leading to the growth of eccentricity and the precession of the disk. This process can be understood through mode coupling: the resonance mode $(m, \ell) = (3, 3)$ excites a tidally induced two-armed mode $(2, 3)$ via its interaction with the eccentric mode $(1, 0)$, which in turn reinforces the disk eccentricity [13]. The precession of the resulting eccentric disk produces the superhump phenomenon observed in SU UMa-type dwarf novae. SPH simulations have previously reproduced this behavior, showing the period decrease from stage A (long-period superhump) to stage B (shorter period) through power spectral analysis

of particle orbits [14–16].

Figure 3 presents the DMD analysis of the same SPH simulation. The upper panels show the surface-density evolution of the disk, with the L_1 point located at the bottom. The disk clearly exhibits off-center eccentricity and precession. The simulation data were converted to a 128×128 spatial grid and 150 temporal frames, and decomposed by DMD into 72 modes. Representative spatial modes and their temporal dynamics are shown in the bottom and middle panels, respectively.

Mode (a) (bottom-left) corresponds to the dynamics shown by the dashed line in the middle panel. It has a triangular pattern characteristic of the (3, 3) resonance mode and appears as a transient component that peaks around time ~ 50 before decaying without oscillation. Two additional oscillatory modes, (b1) and (b2), exhibit spiral-like and elliptical patterns, respectively, suggesting a developing elliptical structure; their combined dynamics (blue line) decay simultaneously with mode (a), indicating that the excitation of the resonance and eccentric modes occurs nearly simultaneously when the disk reaches the resonance radius. Later in the evolution, oscillatory modes (c1) and (c2) (red line) become dominant. Mode (c1) shows a clear off-center oscillation, while mode (c2) represents its second harmonic, indicating a well-developed elliptical disk. The characteristic periods of modes (b1) and (c1), $19.3, P_{\text{orb}}$ and $31.5, P_{\text{orb}}$, respectively, can be interpreted as the precession periods of the disk. Because a longer precession period corresponds to a shorter superhump period, the early transient mode is associated with the stage A superhump, while the later quasi-steady mode corresponds to the stage B one.

This analysis demonstrates that DMD can reproduce known dynamical features while also providing additional insight into the spatiotemporal evolution of complex systems. Unlike traditional power spectral analyses of particle trajectories, DMD directly reveals the evolution of transient and oscillatory modes in space and time, offering a more comprehensive view of the system’s dynamics.

5. Machine classification and autonomous observation systems

Modern wide-field surveys detect a large number of transient events every night. To handle this flood of detections, machine learning methods — such as deep learning — are widely used to distinguish real transients from bogus candidates [17]. Once a newly detected signal is confirmed as real, classification models such as random forests are applied to estimate its variable star type [18]. Based on the classification result, appropriate follow-up observations can be initiated, and the observing mode is selected according to the expected nature of the target.

The 1.5-m "Kanata" optical and near-infrared telescope, located in Hiroshima, is dedicated to rapid follow-up observations of transient objects. For example, spectroscopic observations are conducted for novae to trace the formation of nova winds, while time-series imaging is performed for dwarf novae to detect evolving ordinary or early superhumps. However, the nature of a newly discovered transient is often uncertain at the time of detection, requiring decisions about the optimal observing mode under uncertainty. Automating this decision-making process presents a major challenge.

To address this issue, we have recently developed an autonomous decision-making system based on the framework of information theory. Here, we consider five possible classes: nova ($k = 1$), dwarf nova (DN; $k = 2$), WZ Sge-type dwarf nova (WZ; $k = 3$), Mira ($k = 4$), and flare star (Flare; $k = 5$). Three observing modes (m) are available with Kanata: (1) multi-band imaging

to measure $B - V$ ($m = 1$), (2) spectroscopy to measure the equivalent width (EW) of $H\alpha$ ($m = 2$), and (3) time-series imaging to detect short-term variability ($m = 3$).

The probability that an object belongs to class k immediately after discovery is given by Bayes' theorem:

$$p_{\mathbf{x}}(k) = p(k|\mathbf{x}) = \frac{p(\mathbf{x}|k)\pi(k)}{\sum_k p(\mathbf{x}|k)\pi(k)}, \quad (7)$$

where \mathbf{x} is the feature vector of the sample. We constructed a training dataset using eight features: Galactic coordinates (ℓ, b), absolute magnitudes at maximum (M_{\max}) and in quiescence (M_{qui}), amplitude (a), and quiescent colors ($g - r, r - i, i - z$). These features were obtained from the AAVSO VSX, Gaia DR3, Pan-STARRS DR1, and SDSS DR16 catalogs. The likelihood functions $p(\mathbf{x}|k)$ are modeled as multivariate normal distributions, and the prior probabilities $\pi(k)$ are assumed to be uniform, $\pi(k) = 0.2$. Thus, we calculate $p_{\mathbf{x}}(k)$ for a newly discovered transient using this Bayesian classifier.

The uncertainty of the classification immediately after discovery can be quantified using Shannon entropy: $H_{\mathbf{x}}(K) = -\sum_k p_{\mathbf{x}}(k) \log_2 p_{\mathbf{x}}(k)$. Let y_m denote the measurement obtained through a follow-up observation with mode m . The updated entropy after obtaining y_m is

$$H_{\mathbf{x}}(K|y_m) = -\sum_k q_{\mathbf{x}}(k|y_m) \log_2 q_{\mathbf{x}}(k|y_m), \quad (8)$$

where

$$q_{\mathbf{x}}(k|y_m) = \frac{q_{\mathbf{x}}(k, y_m)}{q_{\mathbf{x}}(y_m)} = \frac{q(y_m|k)p_{\mathbf{x}}(k)}{\sum_k q(y_m|k)p_{\mathbf{x}}(k)}. \quad (9)$$

Although $H_{\mathbf{x}}(K|y_m)$ can only be evaluated after the measurement of y_m , its expected value, or conditional entropy, can be estimated in advance as

$$H_{\mathbf{x}}(K|Y_m) = \int q_{\mathbf{x}}(y_m) H_{\mathbf{x}}(K|y_m) dy_m = -\int \sum_k q_{\mathbf{x}}(k, y_m) \log_2 \frac{q_{\mathbf{x}}(k, y_m)}{q_{\mathbf{x}}(y_m)}. \quad (10)$$

Here, $q(y_m|k)$ represents the distribution of the observable y_m for each class — for instance, the distribution of $B - V$ for DNe or that of EW($H\alpha$) for novae — derived from the training dataset. The information gain (or mutual information) of mode m is then defined as $I_{\mathbf{x}}(K; Y_m) = H_{\mathbf{x}}(K) - H_{\mathbf{x}}(K|Y_m)$. The optimal observing mode, m is selected as the one that maximizes $I_{\mathbf{x}}(K; Y_m)$.

This system has been implemented on the Kanata telescope and is referred to as Smart Kanata [19]. Figure 4 shows examples of its application. For instance, TCP J20522886+1638203 was discovered with a large outburst amplitude ($\gtrsim 9$ mag) and a low galactic longitude. The classifier gave the highest probability to WZ, but a non-negligible one to Nova. Consequently, Smart Kanata selected the spectroscopic mode ($m = 2$) to measure the EW of $H\alpha$, which yielded the highest expected information gain. Although observations were disrupted by poor weather, the object was later confirmed as a WZ Sge-type dwarf nova. Another example is TCP J08374922+0134065. Because of its low luminosity, the probabilities for Nova and Mira were low, while those for DN, WZ, and Flare were comparable. Smart Kanata automatically selected the multi-band imaging mode

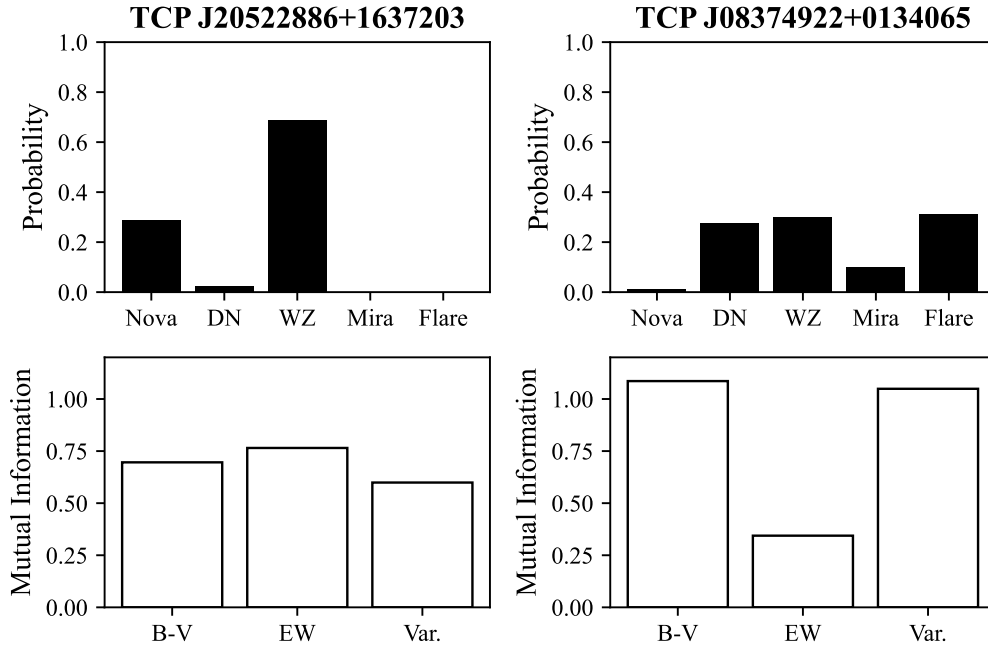


Figure 4: Examples of Smart Kanata targets. Upper and lower panels show class probabilities and mutual information, respectively.

($m = 1$), obtained $B - V = 0.40$, and updated the class probabilities, yielding $p_{\text{DN}} = 0.84$. As the probabilities for Nova and WZ dropped significantly, the system automatically terminated further observations. These examples demonstrate that Smart Kanata can make observation decisions comparable to those of domain experts.

6. Summary

Appropriate modeling and use of machine learning techniques enable us to infer hidden structures in accretion disks and flows from limited data (inverse problems in Section 2), indirect data (state-space models in Section 3), overly high-dimensional data (DMD in Section 4), and a large number of targets (autonomous observation system in Section 5). Some of the methods introduced in this article are fundamental and have long been used in other fields, and they are easy to implement with modern python packages, such as LASSO regression with `sklearn.linear_model.Lasso` and DMD with `PyDMD`. While the state-space model in Section 3 was constructed specifically for X-ray rapid variability using `tensorflow_probability`, such probabilistic programming frameworks can serve as powerful and flexible tools for estimating latent structures.

Such approaches will continue to play an important role in uncovering the underlying mechanisms of accretion and variability in the coming era of data-rich astronomy.

References

- [1] T.R. Marsh and K. Horne, *Images of accretion discs - II. Doppler tomography.*, *MNRAS* **235** (1988) 269.
- [2] K. Horne, *Images of accretion discs -I. The eclipse mapping method.*, *MNRAS* **213** (1985) 129.
- [3] R. Tibshirani, *Regression shrinkage and selection via the lasso*, *Journal of the Royal Statistical Society Series B: Statistical Methodology* **58** (1996) 267.
- [4] T. Kato and M. Uemura, *Period Analysis using the Least Absolute Shrinkage and Selection Operator (Lasso)*, *PASJ* **64** (2012) 122 [1205.4791].
- [5] M. Uemura, T. Kato, D. Nogami and R. Mennickent, *Doppler tomography by total variation minimization*, *PASJ* **67** (2015) 22 [1412.5528].
- [6] M. Honma, K. Akiyama, M. Uemura and S. Ikeda, *Super-resolution imaging with radio interferometry using sparse modeling*, *PASJ* **66** (2014) 95.
- [7] Event Horizon Telescope Collaboration, K. Akiyama, A. Alberdi, W. Alef, K. Asada, R. Azulay et al., *First M87 Event Horizon Telescope Results. IV. Imaging the Central Supermassive Black Hole*, *ApJL* **875** (2019) L4 [1906.11241].
- [8] A. Veledina, *Interplay of spectral components in timing properties of accreting compact objects*, *MNRAS* **481** (2018) 4236 [1809.06053].
- [9] T. Omama, *Joint Analysis of X-ray Spectral and Timing using the State-Space Model: Application for the Black Hole Binary MAXI J1820+070*, Ph.D. thesis, The Graduate University for Advanced Studies, SOKENDAI, 2024.
- [10] P.J. Schmid, *Dynamic mode decomposition of numerical and experimental data*, *Journal of fluid mechanics* **656** (2010) 5.
- [11] R. Whitehurst, *Numerical simulations of accretion discs - I. Superhumps : a tidal phenomenon of accretion discs.*, *MNRAS* **232** (1988) 35.
- [12] Y. Osaki, *A Model for the Superoutburst Phenomenon of SU Ursae Majoris Stars*, *PASJ* **41** (1989) 1005.
- [13] S.H. Lubow, *Simulations of Tidally Driven Eccentric Instabilities with Application to Superhumps*, *ApJ* **381** (1991) 268.
- [14] J.R. Murray, *Simulations of superhumps and superoutbursts*, *MNRAS* **297** (1998) 323 [astro-ph/9710233].
- [15] T. Kato, A. Imada, M. Uemura, D. Nogami, H. Maehara, R. Ishioka et al., *Survey of Period Variations of Superhumps in SU UMa-Type Dwarf Novae*, *PASJ* **61** (2009) S395 [0905.1757].

- [16] T. Kato and Y. Osaki, *New Method of Estimating Binary's Mass Ratios by Using Superhumps*, *PASJ* **65** (2013) 115 [1307.5588].
- [17] D.A. Duev, A. Mahabal, F.J. Masci, M.J. Graham, B. Rusholme, R. Walters et al., *Real-bogus classification for the Zwicky Transient Facility using deep learning*, *MNRAS* **489** (2019) 3582 [1907.11259].
- [18] T. Jayasinghe, C.S. Kochanek, K.Z. Stanek, B.J. Shappee, T.W.S. Holoiien, T.A. Thompson et al., *The ASAS-SN catalogue of variable stars I: The Serendipitous Survey*, *MNRAS* **477** (2018) 3145 [1803.01001].
- [19] M. Uemura, Y. Koga, R. Sazaki, T. Yukino, T. Nakaoka, R. Imazawa et al., *Smart Kanata: A framework for autonomous decision-making in rapid follow-up observations of cataclysmic variables*, *PASJ* **77** (2025) 219 [2412.02092].